RSC Advances

PAPER

View Article Online
View Journal | View Issue

Cite this: *RSC Adv.*, 2017, **7**, 46297

Excellent mechanical performance and enhanced dielectric properties of OBC/SiO_2 elastomeric nanocomposites: effect of dispersion of the SiO_2 nanoparticles†

Xing Zhao, Lu Bai,* Rui-Ying Bao, Zheng-Ying Liu, Ming-Bo Yang and Wei Yang*

Two kinds of fumed SiO_2 nanoparticles with the same average diameter but distinct surface characteristics (hydrophilic A200 and hydrophobic R974) were incorporated into an ethylene-α-olefin block copolymer (OBC) to prepare high-performance thermoplastic elastomeric nanocomposites *via* simple melt mixing. Hydrophilic A200 exhibits a particular chain-like distribution while hydrophobic R974 shows a homogenous dispersion in the nanocomposites. The rheological percolation threshold of OBC/A200 nanocomposites was much lower than that of OBC/R974 nanocomposites, showing a more developed nanoparticle network in OBC/A200 nanocomposites. Thermodynamic analysis revealed that the particular chain-like distribution of A200 and more developed network structure are due to the selective localization of hydrophilic A200 in the melt. The reinforcement effect of hydrophilic A200 in OBC/A200 nanocomposites is always higher than that of hydrophobic R974 in OBC/R974 nanocomposites at the same filler loading, and even better, the increments in the tensile modulus of OBC/A200 nanocomposites are almost four times higher than that of OBC/R974 nanocomposites at the same silica loading. Besides, the dielectric permittivity of the OBC/A200 composite at low frequency was also higher than that of the OBC/R974 composite with the same loading of filler at the same frequency. These results provide guidance for the preparation of high-performance elastomeric nanocomposites with both excellent mechanical performance and enhanced dielectric properties.

Received 21st July 2017
Accepted 25th September 2017

DOI: 10.1039/c7ra08074c

rsc.li/rsc-advances

Introduction

In recent years, nanofiller modified thermoplastic elastomers have emerged as a novel class of nanocomposites and have attracted considerable interest. Especially, functional thermoplastic elastomer nanocomposites with high conductivity, dielectric properties, flame-retardant performance and so on, have achieved significant progress.[1–8] The matrices for thermoplastic elastomer nanocomposites include styrenic block copolymers, thermoplastic polyolefins, thermoplastic polyurethanes and thermoplastic copolyesters, *etc.*[7–10] These thermoplastic elastomers generally show both good processability and high elasticity which impart a favorable application prospect to their nanocomposites.

High-performance thermoplastic elastomer nanocomposites have been developed with the addition of a variety of inorganic fillers such as silica nanoparticles (NPs), graphene, carbon black, carbon nanotubes, ceramics and other nanomaterials.[10–16] However, these nanomaterials are generally poorly dispersed within the matrix in the form of aggregates. It has been widely accepted that a homogeneous and uniform dispersion of NPs is one of the keys to achieve excellent reinforcement in physical and functional performance of thermoplastic elastomer nanocomposites.[17,18] Many efforts have been devoted to improve the dispersion of nanomaterials by mixing methods, surface modification of nanomaterials and other methods.[19–22]

Fumed silica NP was one of the most widely used nano fillers for nanocomposites because of the high specific surface area, high thermal stability and high mechanical strength.[23–28] Abundant silanols exist on the surface of silica NPs,[29] which lead to the dispersion of silica NPs in the form of aggregates in the matrix due to the powerful NP–NP interaction and hydrogen bonding interactions. Thus, silica NPs are generally modified with different functional groups in order to achieve uniform dispersion by increasing NP–matrix interaction and decreasing NP–NP interaction.[30,31] Except for reinforcement for thermoplastic elastomers, silica NPs are also utilized to fabricate dielectric composite materials. It has been reported that the addition of silica NPs in polymer can obtain high-k polymer

College of Polymer Science and Engineering, Sichuan University, State Key Laboratory of Polymer Materials Engineering, Chengdu, 610065, Sichuan, China. E-mail: slulu_1116@163.com; weiyang@scu.edu.cn; Fax: +86 28 8546 0130; Tel: +86 28 8546 0130

† Electronic supplementary information (ESI) available. See DOI: 10.1039/c7ra08074c

composites which provide an ideal solution to combine the dielectric property of fillers and low-temperature process-ability of polymer matrix.[32] However, high filler loadings reduces processability of the composites and even leads to a decrease in dielectric permittivity because NPs trend to agglomerate at high filler loading. In this regard, homogenous dispersion of silica NPs is still an important issue for preparation of high-k polymer composites.

Recently, a novel class of ethylene-α-olefin copolymers, olefin block copolymers (OBCs), which consist of alternating hard segments (crystallizable ethylene-α-olefin blocks with extremely low levels α-olefin comonomer) and soft segments (amorphous ethylene-α-olefin blocks with high levels of α-olefin comonomer) have been synthesized by the chain shuttling technology.[33–35] Based on this technology, the produced OBCs feature excellent elastomeric property, good processability, outstanding heat resistance and high thermal stability. Moreover, OBCs exhibit better crystallization ability, higher crystallization temperature (T_c) and melting temperature (T_m), compared with ethylene-α-olefin random copolymers (ORCs, one of the most widely used elastomeric polymers), resulting in a significantly promising applications at relative higher temperatures.[36,37] With these advantages, OBCs are chosen as the matrix to prepare multi-functional thermoplastic elastomer nanocomposites.[37–39] In our previous work, the mechanical properties of OBC were enhanced by introduction of multi-walled carbon nanotubes (MWCNTs).[37] An extremely uniform dispersion of MWCNTs in OBC through melt mixing was achieved due to the selective localization of MWCNTs caused by lower affinity towards the hard blocks of OBC. As the result, the mechanical properties of OBC were evidently improved.

In the present study, to impart enhanced mechanical and dielectric performances of OBC-based nanocomposites, two kinds of fumed silica NPs with the same average diameter but distinct surface characteristics (hydrophilic and hydrophobic) were incorporated into OBC *via* simple melt mixing. Scanning electron microscope (SEM) and transmission electron microscope (TEM) were carried out to characterize the different dispersion states of different silica NPs in the solid state, and rheological measurements along with thermodynamic analysis were performed to reveal the different dispersion states of silica NPs in the molten state. A chain-like dispersion of hydrophilic silica nanoparticles (A200) was achieved since the A200 NPs exhibit different affinity towards the different blocks of OBC, while hydrophobic R974 NPs dispersed randomly in OBC. As a result, the two series of OBC-based nanocomposites exhibit distinctly different mechanical and dielectric properties.

Experimental

Materials

OBC (Infuse 9500), synthesized by chain shuttling polymerization technology, consisting of nearly amorphous soft segments and crystallizable hard segments, with a total octene content of 38%, was purchased from Dow Chemical Co. (Midland, MI, USA). The weight-average molecular mass (M_w), polydispersity (M_w/M_n) and density of OBC are 82 600 g mol^{-1}, 2.3 and 0.878 g cm^{-3}, respectively. Two kinds of fumed silica NPs produced by Evonik Degussa, with distinct surface characteristics but the same average diameter of 12 nm were used. One is hydrophilic silica NPs, A200, with a hydroxyl density of 2.5 –OH per nm^2 and the other is hydrophobic silica NPs, R974, synthesized by the replacement of methyl for half of hydroxyl present on surface of A200, namely, with a methyl density of 1.25 –CH_3 per nm^2.

Sample preparation

OBC-based nanocomposites filled with R974 and A200 respectively, were prepared by simple melt mixing in the mixer of a torque rheometer (XSS-300, Shanghai Kechuang Rubber Plastics Machinery Set Ltd, Shanghai, PR China) with a rotational speed of 50 rpm at 150 °C for 5 min. The resulted samples were designated as OBC–R-*x* and OBC–A-*x* respectively, where R and A refer to the two kinds of fumed SiO_2 NPs, and *x* stands for the volume fraction of silica in the composites. After compounding, all the composites were compression molded into sheets with a thickness of about 1.2 mm at 150 °C for 3 min under a pressure of 10 MPa.

Characterization

Morphological observation. The morphology and dispersion states of silica NPs in the thermoplastic elastomer nanocomposites were observed with a JEOL JSM-5900LV scanning electron microscope (SEM, JEOL, Japan) at an accelerating voltage of 20 kV. The compression-molded samples were immersed in liquid nitrogen for 1 h, and then quickly impact fractured. All the fractured surfaces were sputtered with gold before observation. Furthermore, the dispersion states of silica nanoparticles were examined with a high-resolution transmission electron microscope (TEM) equipped with a field emission gun operating at 200 kV. Before observation, ultrathin sample sections with a thickness of 50–100 nm were cryomicrotomed on a Leica EM UC6 ultra-microtome at −120 °C.

Dielectric measurements. Dielectric properties of OBC and its nanocomposites were determined by an impedance analyzer (German Novocontrol, Concept 50) at a voltage of 1 V and a frequencies range of 10^0 to 10^7 Hz. The samples for dielectric tests were prepared by thermally compressing OBC and the composites into sheets with a thickness of about 1.2 mm and diameter of 25 mm at 150 °C for 3 min under a pressure of 10 MPa.

Dynamic rheological measurements. Rheological measurements were performed on a stress-controlled rotational rheometer (AR2000EX, TA Instruments, USA) using a parallel plate geometry with a 25 mm diameter. Frequency sweep was carried out in a dynamic frequency range of 0.01–100 Hz at a strain of 1% within the linear viscoelastic region at 150 °C under nitrogen atmosphere. The samples were prepared by thermally compressing the composites into round disks with a thickness of 1.2 mm and diameter of 25 mm at 150 °C for 3 min under a pressure of 10 MPa.

Mechanical properties. The mechanical performance tests under uniaxial tension were performed on an Instron 5967

universal material testing machine at room temperature with a gauge length of 25 mm, and the rate of tension was 100 mm min^{-1}. All the tensile specimens were dumb-bell ones with a dimension of 25 mm × 4 mm × 0.5 mm, cut from the compression-molded sheets with a thickness of about 0.5 mm. At least five specimens were tested for each measurement and the average results were reported. Before measurement, all the specimens were stored at room temperature for one week.

Results and discussion

Dispersion of silica nanoparticles in OBC/SiO_2 nanocomposites

The dispersion states of both SiO_2 NPs in OBC matrix were observed by SEM and TEM. The SEM images of the nanocomposites with relatively low (5 vol%) and high (15 vol%) contents of SiO_2 are shown in Fig. 1a–f. In the whole field of vision, no large aggregates can be found in neither OBC/A200 nor OBC/R974 nanocomposites. A200 SiO_2 NPs show a greater degree of connection in OBC/A200 nanocomposites as indicated in Fig. 1a, c and e, while single R974 NP and their small aggregates are uniformly dispersed in the matrix as shown in Fig. 1b, d and f because of the poor NP–NP interactions.[40] The dispersion was also examined by TEM. Fig. 1g confirms that a chain-like network structure was formed in OBC/A200 nanocomposites, while R974 NPs were irregularly dispersed in OBC/R974 nanocomposites as shown in Fig. 1h. The reason for the chain-like dispersion in OBC/A200 will be analyzed in detail in the following section.

Dielectric properties

Fig. 2 depicts the dielectric permittivity and loss tangent of OBC/A200 and OBC/R974 nanocomposites with different content of SiO_2 as a function of frequency from 10^0 Hz to 10^7 Hz. In the low frequency ranges, the dielectric permittivity of OBC/A200 nanocomposites decreased sharply with the increasing of frequency owing to remarkable dielectric relaxation from 10^0 to 10^3 Hz. In the high frequency ranges, dielectric permittivity of OBC/A200 nanocomposites gradually become stable, because the dipoles do not have time to align in the direction of applied external field.[41] The dielectric permittivity of OBC/R974 nanocomposites shows a substantial independence of frequencies. The dielectric loss of both OBC/A200 and OBC/R974 nanocomposites is quite low, always lower than 1 in the entire range of frequencies even when the content of SiO_2 is as high as 20 vol%.

The dielectric permittivity and loss tangent at 1 Hz of OBC/A200 and OBC/R974 nanocomposites are summarized as a function of SiO_2 content in Fig. 3. The dielectric permittivity of OBC/A200 nanocomposites continuously increased from 3.1 to 16.5 with increasing SiO_2 content. However, the dielectric permittivity for OBC/R974 nanocomposites shows very slight change with the increasing of SiO_2 content. The dielectric loss tangent of all OBC/A200 nanocomposites is higher than that of pure OBC, while the dielectric loss tangent of all OBC/R974 nanocomposites shift to a lower value compared with pure OBC as shown in Fig. 3b.

The different performances in dielectric properties for two series of nanocomposites can be ascribed to the different surface characteristics and the distinct dispersion states of SiO_2 nanoparticles. The surface of A200 NPs possesses more polar hydroxyl groups, resulting in effective orientation polarization within the nanocomposites due to the inherent dipolar nature of hydroxyl groups, which directly results in an obvious increase in dielectric permittivity for OBC/A200 nanocomposites at low frequency due to the accumulation of mobile charges at the interface between samples and electrodes. However, the polarization of hydroxyls on surface of R974 NPs was weaken by the numerous methyl surrounding hydroxyls. The addition of silica generally leads to improved dielectric permittivity. However, the groups on the surface of nanoparticles increase free volume at the interface between nanoparticles and matrix, which reduces the dielectric permittivity of the composite.[42] It is also probable reason here. The continuous chain-like distribution of hydrophilic SiO_2 (A200) in the nanocomposites resulting in easier shift of charge carriers to dissipate energy, which would be the main reason for the increase of dielectric loss after the addition of SiO_2 (A200). In this regard, compared with pure OBC, the dielectric loss of OBC/R974 nanocomposites decreases owing to the irregularly-dispersed state of hydrophobic SiO_2 NPs (R974) in OBC/R974 nanocomposites. The weak connection between R974 NPs generates little polarization loss.

Rheological behaviors

Dynamical rheological measurements were utilized widely to characterize the filler network and the phase morphology in polymer composites. It has been admitted that particle-filled polymers can manifest a liquid–solid transition because of the existence of filler network structure within the composites.[43,44] The large-scale relaxation of polymer chains in the composites is prominently restricted by the presence of network structure.[45,46] Thus, rheological properties can reflect the dispersion states of NPs in composites. The storage modulus (G') and loss tangent (tan δ, defined as the ratio of storage modulus to loss modulus) as a function of frequency measured at 150 °C are shown in Fig. 4. It is obvious that the two series of nanocomposites show significantly different rheological properties and the differences can only stem from the different dispersion states of SiO_2 NPs with distinct surface characteristics. Fig. 4a shows that with increasing loading of SiO_2 NPs, the storage modulus of both series of nanocomposites increase gradually, resulting from the restriction of polymer chain relaxation in the presence of rigid particles and formation of inter-connected SiO_2 network. When the content of SiO_2 is as high as 10 vol%, the frequency-dependent of G' in low-frequency region is significantly depressed. It should be noted that the storage modulus of OBC/A200 nanocomposites is always higher than that of OBC/R974 nanocomposites at the same loading level of SiO_2 NPs and the same frequency. The emergence of plateau in the low frequency region of storage modulus *vs.* frequency curve indicates the formation of developed interconnected SiO_2 network structure. Typically, the slopes in the low frequency region of $\lg G' \sim \lg \omega$ curve of OBC–A-5 nanocomposite is 0.157,

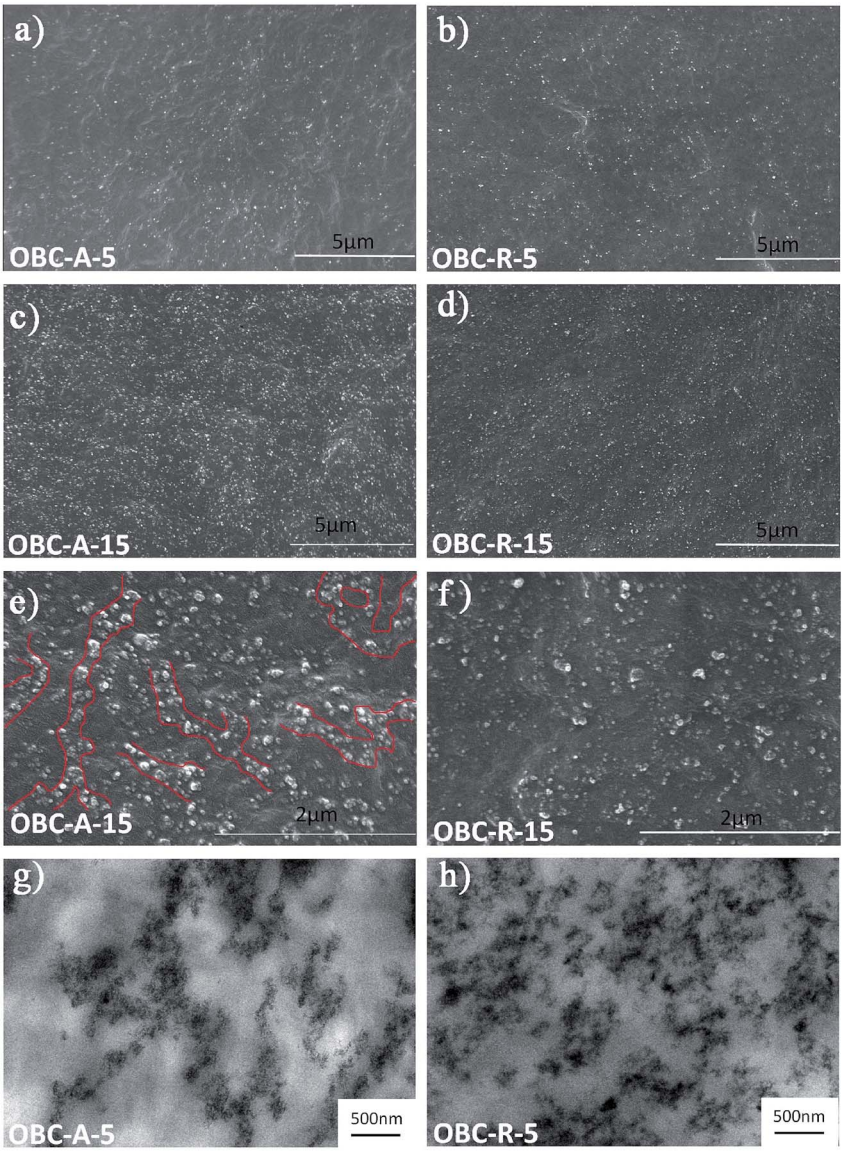

Fig. 1 Typical SEM micrographs of nanocomposites (a) OBC–A-5, (b) OBC–R-5, (c and e) OBC–A-15, (d and f) OBC–R-15, and typical TEM images of nanocomposites (g) OBC–A-5, (h) OBC–R-5.

tremendously lower than that of $\lg G' \sim \lg \omega$ curve of OBC–R-5 (0.582), confirming that the formation of developed network structure containing interconnected hydrophilic SiO_2 NPs in the composites. These results are perfectly consistent with SEM observation as well as the above discussed dielectric properties.

Loss tangent ($\tan \delta$) also characterizes the viscoelastic behavior of materials. In general, a higher value of $\tan \delta$ indicates larger viscosity of the material and a lower value of $\tan \delta$ implies that the material exhibits greater elasticity and less loss of energy under the dynamic deformation. Fig. 4b demonstrates the loss tangent ($\tan \delta$) of OBC/A200 and OBC/R974 nanocomposites with different content of SiO_2 as a function of frequency. Obviously, the $\tan \delta$ of OBC–A-5 is much lower than 1, whereas that of OBC–R-5 is higher than 1, suggesting a significantly solid-like behavior of OBC/A200 nanocomposites. This result also indicates that a developed interconnected network structure was formed at a low loading of hydrophilic SiO_2 (A200) in the nanocomposites, while the hydrophobic SiO_2 (R974) in OBC/R974 nanocomposites presents a separately-dispersed state as shown in Fig. 1.

Thermodynamics analysis

Thermodynamics governs the distribution of the filler in OBC at the equilibrium state and classical thermodynamics can be used to predict the preferential distribution of fillers in OBC.[37] As is known, different from ORC mainly containing random ethylene-α-octene copolymer, OBC consists of alternating hard segments (polyethylene-rich domains) and soft segments (ethylene-α-octene-rich domains).[47] These two kinds of domains present different surface energy (γ), due to the different chain sequences in the domains. Thus, the affinity between SiO_2 NPs

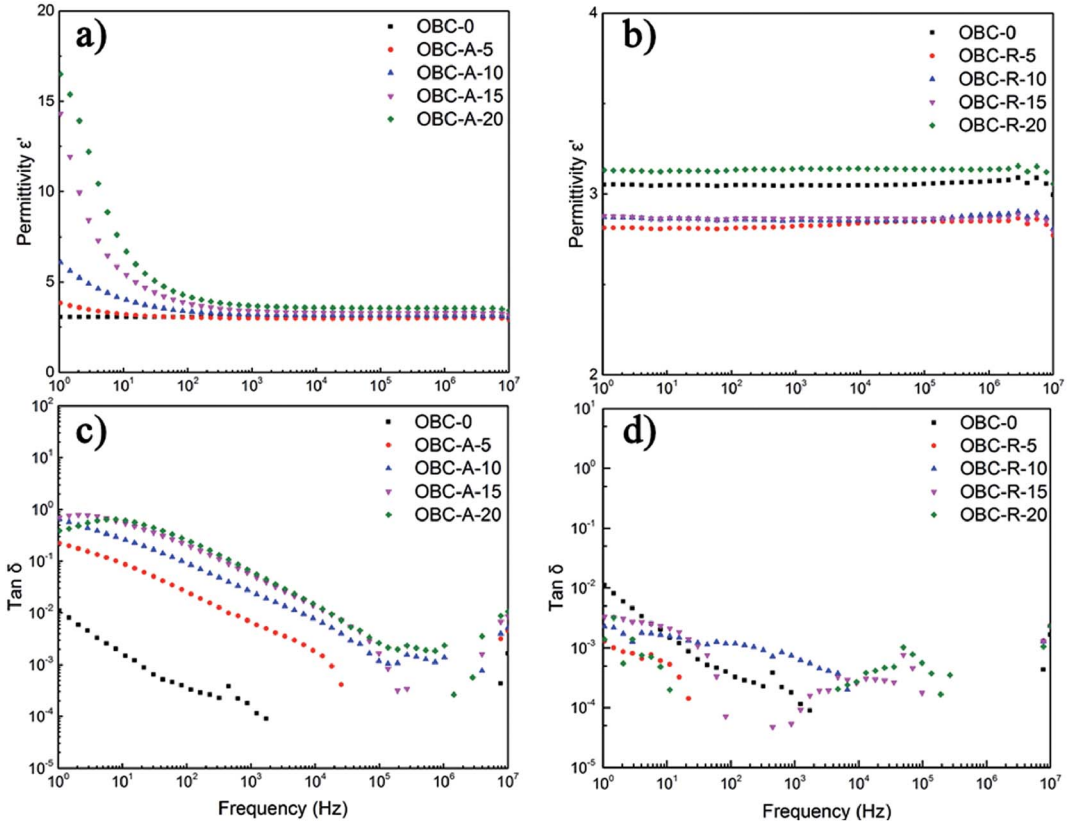

Fig. 2 Frequency responses of (a and b) the dielectric constant, (c and d) dielectric loss of OBC/A200 and OBC/R974 nanocomposites, respectively.

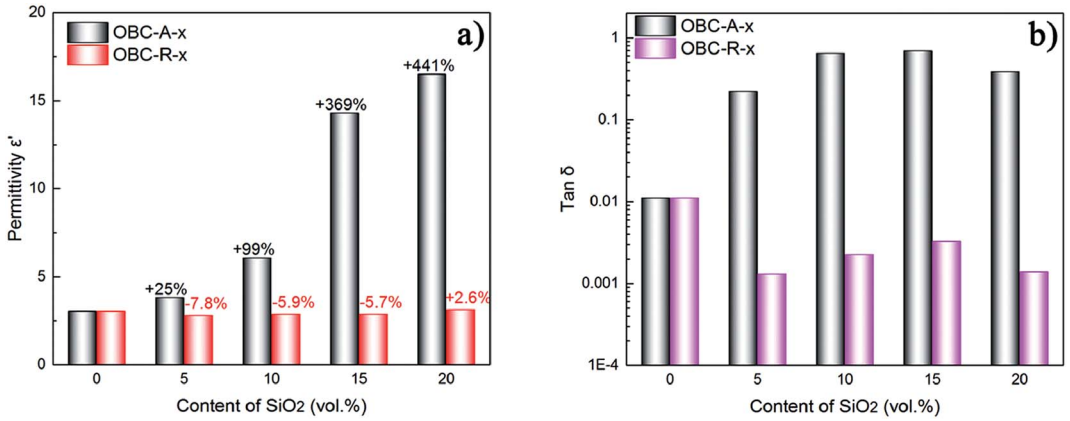

Fig. 3 (a) Dielectric permittivity and (b) dielectric loss for OBC/R974 and OBC/A200 nanocomposites at 1 Hz.

and different domains is possibly the foremost reason for the peculiar chained distribution of hydrophilic SiO_2 in OBC/A200 nanocomposites. Therefore, classical thermodynamics were used to calculate the affinity of different SiO_2 NPs to different domains of OBC.

The estimation of the interfacial tension between two components can be calculated from surface tension using the well-known equation of Wu:[48]

$$\gamma_{1-2} = \gamma_1 + \gamma_2 - 2\left(\sqrt{\gamma_1^d \gamma_2^d} + \sqrt{\gamma_1^p \gamma_2^p}\right)$$

in which γ_{1-2} is the interfacial tension between two components; γ_1 and γ_2 are the surface tension of component 1 and 2; γ_1^d and γ_2^d are dispersion components of the surface tension of component 1 and 2; γ_1^p and γ_2^p are polar components of surface tension of component 1 and 2.

Because of the long polyethylene segments and random ethylene-α-octene segments of OBC, we describe the surface

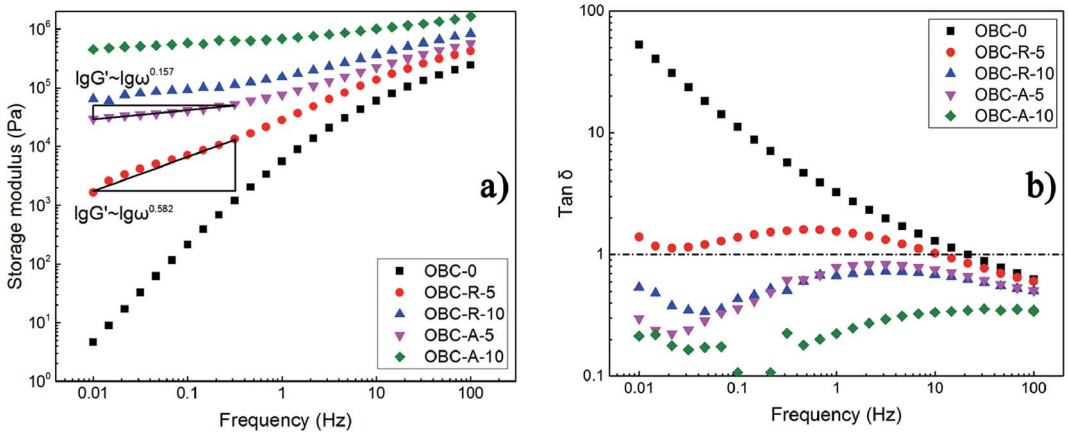

Fig. 4 Logarithmic plots of (a) the storage modulus and (b) the loss tangent as a function of frequency.

tension of polyethylene-rich domains and ethylene-α-octene-rich domains by that of polyethylene and ethylene-octene copolymers (ORCs), respectively. In previous work, it has been proved that the content of octene has little effect on the surface tension of ORCs, thus the use of surface tension of ORC with 39% octene content to describe the surface tension of ethylene-α-octene-rich domains of OBC with 38% octene content is comparatively reasonable.[37] The surface tension values of the materials at 190 °C (higher than the melting point of OBC) were used. The values of surface tension, as well as its dispersion components and polar components are listed in Table 1. The interfacial tension between different SiO_2 NPs and different rich domains of OBC was calculated using the geometric mean equation and the values of all possible pairs are listed in Table 2.

As is known, hydrophilic SiO_2 NPs, A200, tend to gather together to form aggregates due to the high interfacial tension and abundant hydroxy groups. On the contrary, hydrophobic SiO_2 NPs, R974, are more likely to disperse in the polymer matrix in the separately-dispersed state because of the relatively low interfacial tension.[51] However, an unexpected result happened in our work that A200 presented a peculiar chained distribution in OBC/A200 nanocomposites instead of gathering into large aggregates. This phenomenon can be explained with the results from the thermodynamic analysis. As can be seen in Table 2, in OBC/A200 nanocomposites, the interfacial tension between A200 NPs and ethylene-α-octene-rich domains is much smaller than that between A200 NPs and polyethylene-rich domains, namely, A200 shows higher affinity to ethylene-α-octene-rich domains. It indicates that after melt mixing, the interconnected A200 NPs are inclined to distribute along the ethylene-α-octene chain segments, resulting in a chained distribution of A200 NPs in the nanocomposites. In comparison, the interfacial tension between R974 NPs and ethylene-α-octene-rich domains is close to that between R974 NPs and polyethylene-rich domains, which indicates that R974 NPs do not show a selective localization in the different domains of OBC. These results indicated by thermodynamic analysis are in good agreement with SEM and TEM observations.

Table 1 Surface tension values of R974, A200 nanoparticles, ethylene-α-octene-rich domains and polyethylene-rich domains of OBC at 190 °C

Materials	Surface tension (mN m^{-1})		
	Total (γ)	Dispersion component (γ^d)	Polar component (γ^p)
R974[a]	41.81	34.34	7.47
A200[b]	77.3	36.5	40.8
Ethylene-α-octene-rich domains[c]	17.5	15.6	1.9
Polyethylene-rich domains[d]	25.9	25.9	0

[a] According to Liu *et al.*[40] [b] According to Liu *et al.*[40] [c] Described with that of ethylene-olefin random copolymers.[49] [d] Described with that of polyethylene.[50]

Mechanical properties

In this study, we incorporated SiO_2 NPs with distinct surface characteristics into OBC, with the purpose of getting a high-performance nanocomposites. Considering that the peculiar chained distribution of A200 NPs and the interconnected network structure are hopeful to improve mechanical properties of nanocomposites, some of the typical mechanical properties of thermoplastic elastomer nanocomposites are further characterized. The representative uniaxial tensile stress–strain curves for

Table 2 Interfacial tension values calculated using geometric mean equation

System	Pairs	Interfacial tension (γ_{1-2}) (mN m^{-1})
OBC/A200	A200/ethylene-α-octene-rich domains	29.5
	A200/polyethylene-rich domains	41.7
OBC/R974	R974/ethylene-α-octene-rich domains	5.5
	R974/polyethylene-rich domains	8.1

OBC and its nanocomposites are presented in Fig. S1.† The average values of tensile modulus, elongation at break, stress at 100% and 500% stretching of two series of nanocomposites are plotted *versus* the content of SiO_2 NPs in Fig. 5.

As shown in Fig. S1,† the stress–strain curves of pure OBC and its nanocomposites are quite different. Pure OBC shows a continuously increasing stress at low strains and strain-hardening at the late stage. However, nearly all of nanocomposites evidently exhibit a yield plateau or necking phenomenon at low strains. This phenomenon can be attributed to the incorporation of fumed SiO_2 NPs which restricts the segmental motion of the matrix in elastic deformation stage. After yield point, the restricted chain segments begin to move, showing strain-softening. It should be noted that OBC/A200 nanocomposites exhibit more obvious strain-softening compared with OBC/R974 nanocomposites, probably due to the more stable interconnected A200 network structure.

In Fig. 5a and b, the stress at a certain stretching (100% and 500%) of both series of nanocomposites, show a significantly increasing tendency with increasing content of SiO_2 NPs. The stress at a certain stretching mainly depends on the network structure of the fillers in the nanocomposites. With the increasing content of SiO_2 NPs in both OBC/A200 and OBC/R974 composites, the net-work structure of the SiO_2 NPs become more and more perfect, which improve the stress. Comparing OBC/A200 with OBC/R974 nanocomposites, the network structure of SiO_2 is well-developed more easily in OBC/A200 due to the peculiar chain-like structure of SiO_2. Thus, the stress at 100% and 500% stretching of OBC/A200 nanocomposites is always much higher than that of OBC/R974 nanocomposites. In addition, the tensile modulus of both series of nanocomposites increases, and the percentages of reinforcement in the tensile modulus of OBC/A200 are almost four times as much as those of OBC/R974 at the same content of SiO_2 as seen in Fig. 5c. Therefore, we can conclude that the greatly enhanced mechanical properties for OBC/A200 nanocomposites over OBC/R974 nanocomposites is primarily due to the peculiar chained distribution and interconnected network of A200 NPs in OBC/A200 nanocomposites. This particular chain structure can hinder the aggregations of hydrophilic SiO_2, and impel SiO_2 to present a peculiar chained distribution in OBC/A200 nanocomposites, showing a significantly reinforcement effect in the nanocomposites. Typically, larger stress and tensile modulus were achieved in OBC/A200 nanocomposites compared with OBC/R974 nanocomposites.

In Fig. 5d, the tensile elongation at break of OBC/A200 and OBC/R974 nanocomposites are both higher than 1300% even when the content of SiO_2 is high as 20 vol%, and the tensile

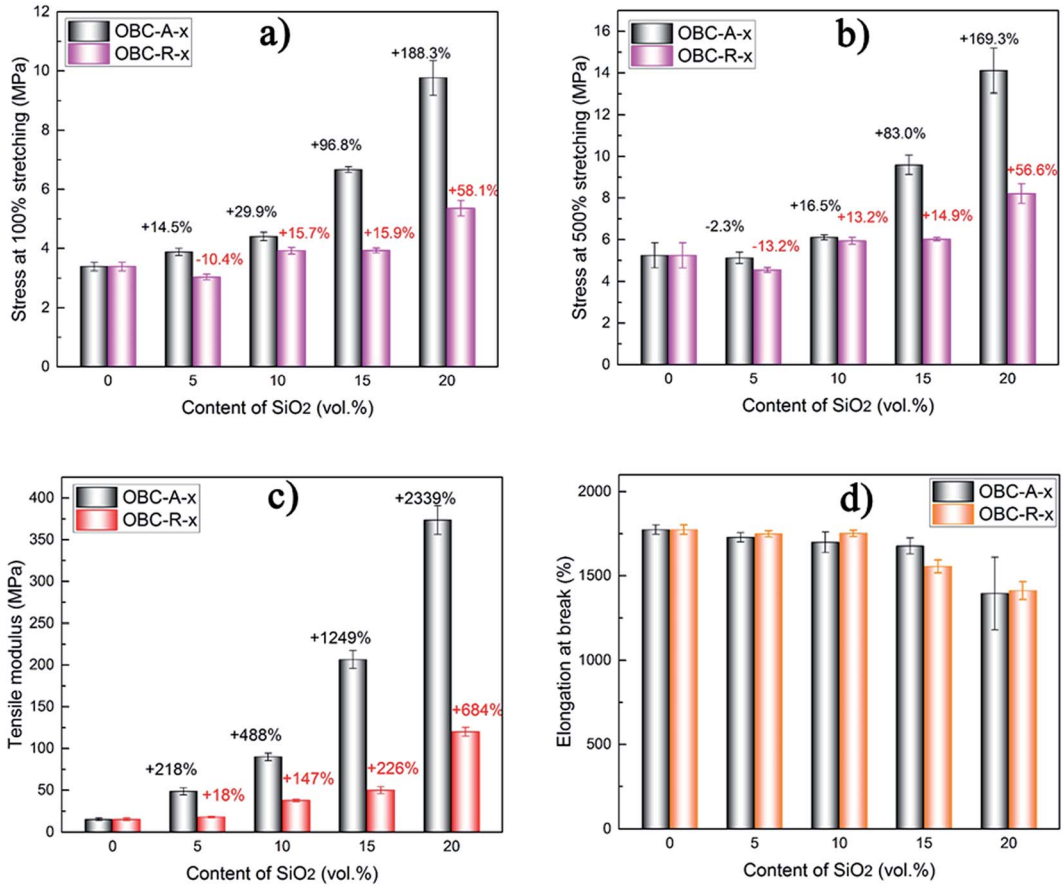

Fig. 5 (a) Stress at 100% stretching, (b) stress at 500% stretching, (c) elongation at break and (d) tensile modulus of OBC/R974 and OBC/A200 nanocomposites as a function of SiO_2. Percentages in (a), (b) and (c) are the percentages of reinforcement in stress at 100% stretching, stress at 500% stretching and tensile modulus, respectively when compared with pure OBC.

elongations at break of both series of nanocomposites are close at the same content of SiO_2. According to previous studies,[52,53] the large elongation at break of OBC stems from the long and flexible chain segments (soft blocks) between crystals (hard blocks), which can be stretched easily.[54]

Thus, a new elastomeric nanocomposite with excellent mechanical strength and toughness, and improved dielectric properties was developed. With these advantages, this new material holds potential to be utilized in fields such as dielectric elastomers, toughening agents for dielectric materials, electrically-driven deformation materials and flexible damping devices.

Conclusions

OBC/A200 and OBC/R974 nanocomposites were prepared through one-step melt compounding method and the effect of the distinct different surface characteristics of the two kinds of fumed nano-silica nanoparticles on the structure and performance of OBC based nanocomposites was investigated. The hydrophilic silica (A200) with more silanols dispersed in OBC in a peculiar chain-like structure while the hydrophobic silica (R974) NPs dispersed separately in OBC. Selective localization of hydrophilic silica (A200) due to the higher affinity towards the soft blocks of OBC dominates the peculiar chain-like distribution of hydrophilic silica in OBC composites while the hydrophobic silica NPs exhibit close affinity towards both the soft blocks and hard blocks of OBC. The percolation threshold of OBC/A200 nanocomposites is lower than that of OBC/R974 nanocomposites due to the peculiar chain-like distribution and inter-connected SiO_2 in OBC/A200 nanocomposites. The OBC/A200 nanocomposites exhibit enhanced dielectric permittivity with low dielectric loss. The percentages of reinforcement in stress at a certain stretching of OBC/A200 nanocomposites are always higher than that of OBC/R974 nanocomposites at the same silica loading, and even better, the percentages of reinforcement in tensile modulus of OBC/A200 nanocomposites are almost four times higher than that of OBC/R974 nanocomposites at the same silica loading.

Conflicts of interest

There are no conflicts to declare.

Acknowledgements

This work was supported by the National Natural Science Foundation of China (NNSFC Grants 51422305, 21374065 and 51503132), Sichuan Provincial Science Fund for Distinguished Young Scholars (2015JQO003).

References

1 W. L. Hu, R. R. Wang, Y. F. Lu and Q. B. Pei, *J. Mater. Chem. C*, 2014, **2**, 1298–1305.
2 K. Shehzad, A. A. Hakro, Y. Zeng, S. H. Yao, Y. Xiao-Hong, M. Mumtaz, K. Nadeem, N. S. Khisro and Z. M. Dang, *Appl. Nanosci.*, 2015, **5**, 969–974.
3 H. G. Wu, P. J. Yao, N. Y. Ning, L. Q. Zhang, H. C. Tian, Y. P. Wu and M. Tian, *RSC Adv.*, 2016, **6**, 32932–32939.
4 O. S. Kwon, D. Lee, S. P. Lee, Y. G. Kang, N. C. Kim and S. H. Song, *RSC Adv.*, 2016, **6**, 59970–59975.
5 F. Jiang, Y. Q. Zhang, C. Fang, Z. K. Wang and Z. G. Wang, *RSC Adv.*, 2014, **4**, 60079–60085.
6 F. Memarian, A. Fereidoon and M. G. Ahangari, *RSC Adv.*, 2016, **6**, 101038–101047.
7 S. T. Liu, M. Tian, B. Y. Yan, Y. Yao, L. Q. Zhang, T. Nishi and N. Y. Ning, *Polymer*, 2015, **56**, 375–384.
8 T. Li, L. F. Ma, R. Y. Bao, G. Q. Qi, W. Yang, B. H. Xie and M. B. Yang, *J. Mater. Chem. A*, 2015, **3**, 5482–5490.
9 E. Helal, L. G. Amurin, D. J. Carastan, R. R. de Sousa Jr, E. David, M. Frechette and N. R. Demarquette, *Polymer*, 2017, **113**, 9–26.
10 L. Y. Ma, B. Yu, X. D. Qian, W. Yang, H. F. Pan, Y. Q. Shi, L. Song and Y. Hu, *Polym. Adv. Technol.*, 2014, **25**, 605–612.
11 S. M. Lai, C. K. Wang and H. F. Shen, *J. Appl. Polym. Sci.*, 2005, **97**, 1316–1325.
12 O. Malay, O. Oguz, C. Kosak, E. Yilgor, I. Yilgor and Y. Z. Menceloglu, *Polymer*, 2013, **54**, 5310–5320.
13 L. Flandin, A. Chang, S. Nazarenko, A. Hiltner and E. Baer, *J. Appl. Polym. Sci.*, 2000, **76**, 894–905.
14 K. S. Lam, Y. W. Wong, L. S. Tai, Y. M. Poon and F. G. Shin, *J. Appl. Phys.*, 2004, **96**, 3896–3899.
15 D. Ponnamma, K. K. Sadasivuni, M. Strankowski, P. Moldenaers, S. Thomas and Y. Grohens, *RSC Adv.*, 2013, **3**, 16068–16079.
16 Y. J. Chen, Y. Li, D. H. Xu and W. T. Zhai, *RSC Adv.*, 2015, **5**, 82034–82041.
17 D. F. Eckel, M. P. Balogh, P. D. Fasulo and W. R. Rodgers, *J. Appl. Polym. Sci.*, 2004, **93**, 1110–1117.
18 L. Bokobza, *Polymer*, 2007, **48**, 4907–4920.
19 C. Xu, K. Ohno, V. Ladmiral and R. J. Composto, *Polymer*, 2008, **49**, 3568–3577.
20 Y. Y. Huang and E. M. Terentjev, *Polymers*, 2012, **4**, 275–295.
21 Z. M. Dang, M. S. Zheng and J. W. Zha, *Small*, 2016, **12**, 1688–1701.
22 S. K. Kumar, N. Jouault, B. Benicewicz and T. Neely, *Macromolecules*, 2013, **46**, 3199–3214.
23 J. P. Sharma and S. S. Sekhon, *Bull. Mater. Sci.*, 2013, **36**, 629–634.
24 H. R. Jung, D. H. Ju, W. J. Lee, X. W. Zhang and R. Kotek, *Electrochim. Acta*, 2009, **54**, 3630–3637.
25 M. Battistella, M. Cascione, B. Fiedler, M. H. G. Wichmann, M. Quaresimin and K. Schulte, *Composites, Part A*, 2008, **39**, 1851–1858.
26 X. Chen, J. Gug and M. J. Sobkowicz, *Compos. Sci. Technol.*, 2014, **95**, 8–15.
27 P. M. Gore, S. Zachariah, P. Gupta and K. Balasubramanian, *RSC Adv.*, 2016, **6**, 105180–105191.
28 N. Katiyar and K. Balasubramanian, *RSC Adv.*, 2015, **5**, 4376–4384.

29 K. M. S. Meera, R. M. Sankar, J. Paul, S. N. Jaisankar and A. B. Mandal, *Phys. Chem. Chem. Phys.*, 2014, **16**, 9276–9288.
30 E. Barna, B. Bommer, J. Kursteiner, A. Vital, O. von Trzebiatowski, W. Koch, B. Schmid and T. Graule, *Composites, Part A*, 2005, **36**, 473–480.
31 M. I. Aranguren, E. Mora, J. V. Degroot and C. W. Macosko, *J. Rheol.*, 1992, **36**, 1165–1182.
32 K. Deshmukh, M. B. Ahamed, K. K. Sadasivuni, D. Ponnamma, M. A. A. AlMaadeed, R. R. Deshmukh, S. K. K. Pasha, A. R. Polu and K. Chidambaram, *J. Appl. Polym. Sci.*, 2017, **134**, 11.
33 D. J. Arriola, E. M. Carnahan, P. D. Hustad, R. L. Kuhlman and T. T. Wenzel, *Science*, 2006, **312**, 714–719.
34 H. P. Wang, D. U. Khariwala, W. Cheung, S. P. Chum, A. Hiltner and E. Baer, *Macromolecules*, 2007, **40**, 2852–2862.
35 V. C. Gibson, *Science*, 2006, **312**, 703–704.
36 F. Zuo, C. Burger, X. M. Chen, Y. M. Mao, B. S. Hsiao, H. Y. Chen, G. R. Marchand, S. Y. Lai and D. Chiu, *Macromolecules*, 2010, **43**, 1922–1929.
37 T. Li, J. H. Pu, L. F. Ma, R. Y. Bao, G. Q. Qi, W. Yang, B. H. Xie and M. B. Yang, *Polym. Chem.*, 2015, **6**, 7160–7170.
38 S. D. Wu, H. Li, G. S. Huang and J. R. Wu, *RSC Adv.*, 2014, **4**, 19024–19033.
39 Z. Z. Tong, B. Zhou, J. Huang, J. T. Xu and Z. Q. Fan, *RSC Adv.*, 2014, **4**, 15678–15688.
40 X.-Q. Liu, Y. Wang, W. Yang, Z.-Y. Liu, Y. Luo, B.-H. Xie and M.-B. Yang, *J. Mater. Sci.*, 2012, **47**, 4620–4631.
41 J. Y. Kim, W. H. Lee, J. W. Suk, J. R. Potts, H. Chou, I. N. Kholmanov, R. D. Piner, J. Lee, D. Akinwande and R. S. Ruoff, *Adv. Mater.*, 2013, **25**, 2308–2313.
42 T. C. Mo, H. W. Wang, S. Y. Chen, R. X. Dong, C. H. Kuo and Y. C. Yeh, *J. Appl. Polym. Sci.*, 2007, **104**, 882–890.
43 M. Abdel-Goad, P. Potschke, D. H. Zhou, J. E. Mark and G. Heinrich, *J. Macromol. Sci., Part A: Pure Appl.Chem.*, 2007, **44**, 591–598.
44 L. J. Romasanta, M. A. Lopez-Manchado and R. Verdejo, *Eur. Polym. J.*, 2013, **49**, 1373–1380.
45 R. Krishnamoorti, A. S. Silva, M. A. Modi and B. Hammouda, *Macromolecules*, 2000, **33**, 3803–3809.
46 P. Thareja and S. Velankar, *Rheol. Acta*, 2007, **46**, 405–412.
47 H. E. Park, J. M. Dealy, G. R. Marchand, J. A. Wang, S. Li and R. A. Register, *Macromolecules*, 2010, **43**, 6789–6799.
48 S. Wu, *J. Macromol. Sci., Rev. Macromol. Chem. Phys.*, 1974, **C10**, 1–73.
49 C. G. Ma, M. Q. Zhang and M. Z. Rong, *J. Appl. Polym. Sci.*, 2007, **103**, 1578–1584.
50 S. Asai, K. Sakata, M. Sumita and K. Miyasaka, *Polym. J.*, 1992, **24**, 415–420.
51 M. Parvinzadeh, S. Moradian, A. Rashidi and M. E. Yazdanshenas, *Appl. Surf. Sci.*, 2010, **256**, 2792–2802.
52 S. Bensason, E. V. Stepanov, S. Chum, A. Hiltner and E. Baer, *Macromolecules*, 1997, **30**, 2436–2444.
53 J. Minick, A. Moet, A. Hiltner, E. Baer and S. P. Chum, *J. Appl. Polym. Sci.*, 1995, **58**, 1371–1384.
54 H. P. Wang, S. P. Chum, A. Hiltner and E. Baer, *J. Appl. Polym. Sci.*, 2009, **113**, 3236–3244.